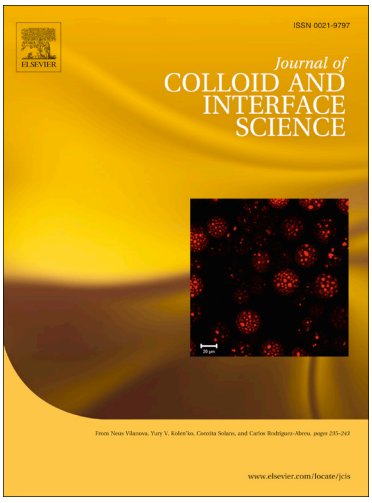

Hierarchical microfibrillar gels from evaporation-induced anisotropic self-assembly of in situ-generated nanocrystals

Hua Wu, Zhengxi Zhang, Stephen Mann, Wuge.H. Briscoe

PII: S0021-9797(19)31153-1
DOI: https://doi.org/10.1016/j.jcis.2019.09.110
Reference: YJCIS 25480

To appear in: *Journal of Colloid and Interface Science*

Received Date: 24 August 2019
Revised Date: 26 September 2019
Accepted Date: 27 September 2019

Please cite this article as: H. Wu, Z. Zhang, S. Mann, Wuge.H. Briscoe, Hierarchical microfibrillar gels from evaporation-induced anisotropic self-assembly of in situ-generated nanocrystals, *Journal of Colloid and Interface Science* (2019), doi: https://doi.org/10.1016/j.jcis.2019.09.110

Hierarchical microfibrillar gels from evaporation-induced anisotropic self-assembly of in situ-generated nanocrystals

Hua Wu[1], Zhengxi Zhang[2], Stephen Mann[1,3], Wuge. H. Briscoe[1*]

[1]School of Chemistry, University of Bristol, Cantock's Close, Bristol BS8 1TS, United Kingdom

[2]School of Chemistry and Chemical Engineering, Shanghai Jiaotong University, Shanghai, 200240, China

[3]Centre for Protolife Research and Centre for Organized Matter Chemistry, School of Chemistry, University of Bristol, Cantock's Close, Bristol BS8 1TS, United Kingdom

*Email: wuge.briscoe@bristol.ac.uk; Tel: +44 (0)117 3318256

Abstract

Whilst nanocrystal gels may be formed *via* destabilization of pre-functionalized nanocrystal dispersions, gelation *via* assembly of unfunctionalized nanocrystals into fibrillar networks remains a significant challenge. Here, we show that gels with hierarchical microfibrillar networks are formed from anisotropic self-assembly of *in situ*-generated mesolamellar nanocrystals upon evaporation of ZnO nanofluids. The obtained gels display the thermo-reversible behavior characteristic of a non-covalent physical gel. We elucidate a three-stage gelation mechanism. In the pre-nucleation stage, the cloudy ZnO nanofluid transforms into a transparent stable suspension, comprising multi-branched networks of aggregates self-assembled from *in situ*-generated layered zinc hydroxide (LZH) nanocrystals upon solvent evaporation. In the subsequent nucleation and anisotropic 1D fibre growth stage, further evaporation triggers nucleation and growth of 1D nanofibers through reorganization of the nanocrystal aggregates, before rapid nanofibre bundling leading to microfibrillar networks in the ultimate gelation stage. Our results provide mechanistic insights for hierarchical self-assembly of nanocrystals into fibrillar gels and open up facile fabrication routes using reactive transition metal-oxide nanofluids for new functional fibres and gels.

Introduction

Nanocrystal gels (NCGs) have been shown to retain desirable nanoscale properties in materials of macroscopic dimensions that can be easily manipulated and processed[1-4]. Supercritical or sublimation solvent drying of such 'wet' NCGs can also generate aerogels with low-density and high inner surface area, attractive in applications such as catalysis, thermoresistors, piezoelectrics,

adsorbents, and sensors. It is thus critical to understand the gelation mechanism of NCGs so that their structures can be optimized for these processes and applications. Based on the types of the stabilizing ligands on pre-formed nanocrystals, several strategies have been developed to induce destabilization of NC dispersions into gels with disordered self-supported networks. Polymer-induced depletion attractions[5] and electrostatic attractions between oppositely charged NCs may drive gelation in colloidal NC suspensions[6]. Gelation of inorganic- or organic-ligand functionalized NCs may be mediated *via* the coordination bonds between the ligands and added ions[7, 8,9]. Photo- and chemical-oxidation to remove the capping agents on quantum-dot nanocrystals (QDNCs) has also been successfully applied in the formation of QD-based gels[10-14].

However, these gelation pathways require complex chemical finetuning of the stabilizing ligands, whose presence in the gel structure may also hinder the accessibility of the active nanocrystal surface. For instance, aerogels obtained from wet NCGs usually contain trace amounts of impurities as a consequence of incomplete removal of the stabilizing ligands[15] and can thus suffer from the reduced performance (*e.g.* in charge transport and catalysis efficacy).

Furthermore, compared to zero-dimensional (0D) NC aerogels, aerogels comprised of one-dimensional (1D) nanomaterials show higher specific surface areas and facilitate more efficient mass transport[16, 17]. 1D nanomaterials also show enhanced optical, electronic and plasmonic properties compared to NCs[18]. Fabrication of 1D NC assemblies typically explores anisotropic interactions mediated by inhomogeneous ligand coverage[19-22], electric dipoles[23, 24] or anisotropic shape[25] of NCs *via* complex processes, and the formation of stable 1D nanomaterial dispersions

remains a significant challenge. Gels with 3D networks of well-defined 1D NC assemblies have not been previously reported.

Certain small molecules, called low-molecular-weight-gelators (LMWGs), can hierarchically assemble into 3D elongated fibrillar networks by non-covalent interactions, resulting in fibrillar gels[26, 27]. The fibre formation is underpinned by the supersaturation-driven nucleation-growth process described by a modified Avrami model adapted from conventional crystallization processes[26, 28-30]. It remains a significant challenge to develop analogous methods for fabricating nanocrystal gels with fibrillar networks assembled from nanocrystals without invoking sophisticated surface functionalization or stabilization ligands.

Here we show that a layered zinc hydroxide nanocrystal (LZH-NC) gel comprising 3D fibril networks can be formed from *slow* evaporation (thus under quasi-equilibrium conditions to suppress solvent flows and instabilities)[31-33] of a ZnO nanofluid in a solvent mixture of chloroform, methanol and isobutylamine. Upon initial evaporation, ZnO nanoparticle hydration-dissolution leads to rapid emergence of layered zinc hydroxide (LZH) nanocrystals (1.8-3.8 nm in size) intercalated with isobutylamine in a transparent stable suspension (TSS). The nanocrystal aggregates in the TSS then self-assemble into dynamic multibranched networks. Upon further evaporation, TSS destabilization triggers nucleation and anisotropic growth of nanofibers through entropy-driven reorganization of the nanocrystal aggregates, analogous to the supersaturation-driven nucleation-growth of low-molecular-weight-gelators (LMWG) nanofibers[29, 30]. Subsequent bundling of these nanofibres leads to the ultimate gelation with 3D rigid microfibrillar networks.

Results and discussion

Thermo-reversible microfibrillar LZH-nanocrystal organogel

Upon slow evaporation for 218.25 h (~9 days), a 20 mL turbid dispersion (1.0 mg/mL ZnO nanoparticles of 5-10 nm in diameter in a mixed chloroform/methanol/isobutylamine solvent; Fig. 1a) transformed into an organogel (~ 4 mL) that could hold its weight under tube inversion (Fig. 1b, c). Cryo-SEM (Fig. 1d) reveals microfibrillar networks throughout the gel matrix with trapped solvent. These microfibres appeared straight and rigid, with a quadrilateral cross section of 1 - 5 μm in width (Fig. 1e, f). The cross-linking between the fibres did not arise from entanglement of flexible fibres or fibre branching, as often observed in supramolecular gels assembled from LMWGs. Instead, the rigid microfibres retained the straight morphology at their junctions. When the 'wet' fibres (with the solvent in the gel removed by centrifugation) were dispersed in methanol by ultrasonication, TEM imaging of the drop-cast dispersion revealed the presence of nanocrystals (Fig. 1g, h) of size of 2.7 ± 1.1 nm (Fig. 1i), which is smaller than the original ZnO nanoparticle size of 5-10 nm (Supplementary Fig. S1)[32]. This indicates that the nanocrystals were basic building units of the organogel.

With the evaporation of an isobutylamine-containing solvent mixture, it is well established from XPS, TGA, FTIR, XRD, and $^{1}H/^{13}C$ NMR ZnO nanoparticles undergo hydration-dissolution reactions facilitated by the entrained water from ambience, and are rapidly transformed into layered $Zn(OH)_2$ (LZH) intercalated with isobutylamine molecules[31-33]. The crucial role of trace amounts of water in facilitating the hydration-dissolution process has also been discussed in these studies.

Here, XRD of the nanocrystals at the evaporation time of 24 h and in the 'wet' microfibres confirms an interlayer *d*-spacing of 13.3 Å (Supplementary Fig. S3), comparable to the reported μGIXRD *d*-spacing value[33]. HRTEM, SAED (Supplementary Fig. S2A, B and F), and XRD (Fig. S3) further indicate that the LZH nanocrystal layer was of MO_6 or CdI_2-type structure with a thickness of 4.8 Å[34, 35] comprising the edge-sharing octahedral LZH layers with Zn^{2+} ions in octahedral coordination[36, 37]. The length of isobutylamine molecule is ~5.03 Å as calculated by Multiwfn software. This is consistent with a hydrophobic isobutyl bilayer of thickness 8.5 Å (*i.e.* 4.25 Å each layer) intercalated between the LZH layers, with the isobutylamine layers likely interdigitated and tilted at an angle α, giving rise to the total *d*-spacing of 13.3 Å. Therefore, the *in-situ* generated LZH nanocrystals as the basic building blocks in the nucleation-fibre growth-gelation process is of the MO_6 or CdI_2-type structure intercalated with a hydrophobic isobutyl bilayer *via* H-bonding with the oxygen atoms (Fig. 4b3). It should be acknowledged that, whilst the intercalation of isobutylamine within LZH nanocrystals facilitated spontaneous anisotropic 1D fibre growth, its effect on the efficacy of any potential application of such fibrillar gels remains to be fully evaluated. Furthermore, use of different amines (with different chain lengths and branching) would also affect their interactions with the nanocrystals and, in turn, the morphology of evaporation-induced self-assembly products (ms in preparation). We also note that slightly different boiling points of chloroform, methanol, and isobutaylamine in the solvent mixture should lead to slightly different evaporation rates. However, it is challenging to ascertain the dynamic composition during evaporation of the mixture, particularly it would also depend on the preferential interactions between the solvent and in situ-generated nanocrystals whose concentration would vary temporally and spatially upon evaporation.

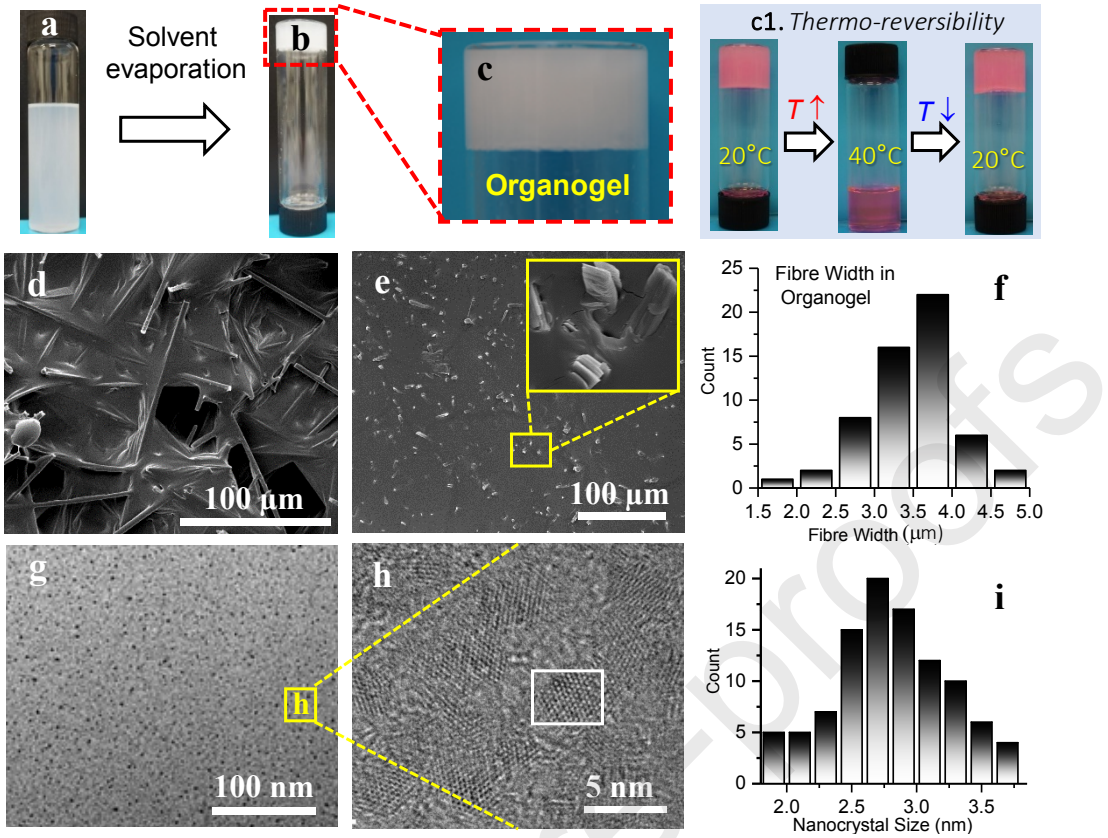

Fig. 1 Organogels characterized by Cryo-SEM and TEM. a, 20 mL ZnO nanofuid in a sealed glass vial: 1.0 mg/mL ZnO nanoparticles (Supplementary Fig. S1) in a mixture of chloroform and methanol (denoted CM; in a volume ratio of $V_C : V_M = 10 : 3$) and also isobutylamine in an overall volume ratio $V_{CM} : V_{iB} = 5 : 1$. **b**, Approximately 4 mL residual gel holding its weight under tube inversion after 218.25 h evaporation at 20 ^{O}C and a relative humidity (RH) ~50% by leaving open the lid of the vial placed in a 128 L cabinet. **c**, Enlarged view of the gel in (**b**). **c1**. Thermoreversibility of microfibrillar oganogel. Gel dyed with 0.005 mg/mL of Sudan I became a transparent solution upon heating to 40 ^{o}C, with the organgel regenerated 15 min after the solution was cooled to 20 ^{o}C. **d**, Cryo-SEM image of the gel microfibrillar networks. **e**, Cryo-SEM image of the cross-section of the gel microfibres, with the inset showing the enlarged view of the yellow-rectangle region. **f**, The width distribution of the microfibres. **g**, TEM image of the nanocrystals from organogel microfibres dispersed in ethanol. **h**. Magnified HRTEM image of the yellow-rectangle region in (**g**) showing several nanocrystals. **i**, The size distribution of nanocrystals in (**d**), in the range of 1.8-3.8 nm. The distribution histograms of the microfibres width and nanocrystal size were obtained by

image analyses using Image J from more than 100 measurements of fibers and nanocrystals.

If the organogel (with Sudan I, a red dye, added to aid visualization) was heated from 20°C at a rate of 1°C min^{-1}, the volume of the transparent liquid phase (sol) gradually increased, and the gel was completely reverted into a transparent liquid at 40°C (Fig. 1c1). Cryo-TEM imaging (Fig. S5c in SI) shows that the nanocrystal aggregate network was already re-formed as soon as the solution was cooled to 20 °C. This means that the microfibrillar gel displays the thermo-reversible behavior characteristic of a non-covalent physical gel, analogous to supramolecular gels obtained from LMWGs by specific non-covalent interactions[26, 27]. Such thermal reversibility has not been reported for nanocrystal gels formed from the interaction of stabilizing ligands of nanocrystals.

Xerogels: Hierarchical microfibrillar structure

Upon evaporative drying of the organogel in Fig. 1c for further 15 days, the dried gel (xerogel) shrank slightly, but largely retained its volume without collapsing (Fig. 2a). The dried quadrilateral microfibres appeared uniform along their entire length (~several mm) (Fig. 2b, c) with a width in the rage 2 - 11 μm (Fig. 2d), compared to the 1 - 5 μm width of the organogel microfibres. This suggests that the fibres in the organogel further assembled into thicker microfibres in the xerogel upon evaporation. The cross-section view of the dried microfibres (Fig. 2e) shows that they were composed of bundles of nanofibers of width 250 nm-300 nm (Fig. 2f). SEM image (Fig. 2g) and TEM image (Fig. 2h) of a fragment from the xerogel reveal that it was packed with aggregates without well-defined boundaries. When the fibres of the dried gel were dispersed in methanol by ultrasonication, TEM imaging of the drop-cast dispersion further reveals the coexistence of

dispersed aggregates and coalesced aggregates (Fig. 2i; white circles in the inset with diameter 9-18 nm). The aggregates were composed of LZH nanocrystals (Fig. 2j) with the same size as those in Fig. 1g, indicating that the microfibers in the organogel comprised bundles of nanofibers assembled from LZH nanocrystal aggregates.

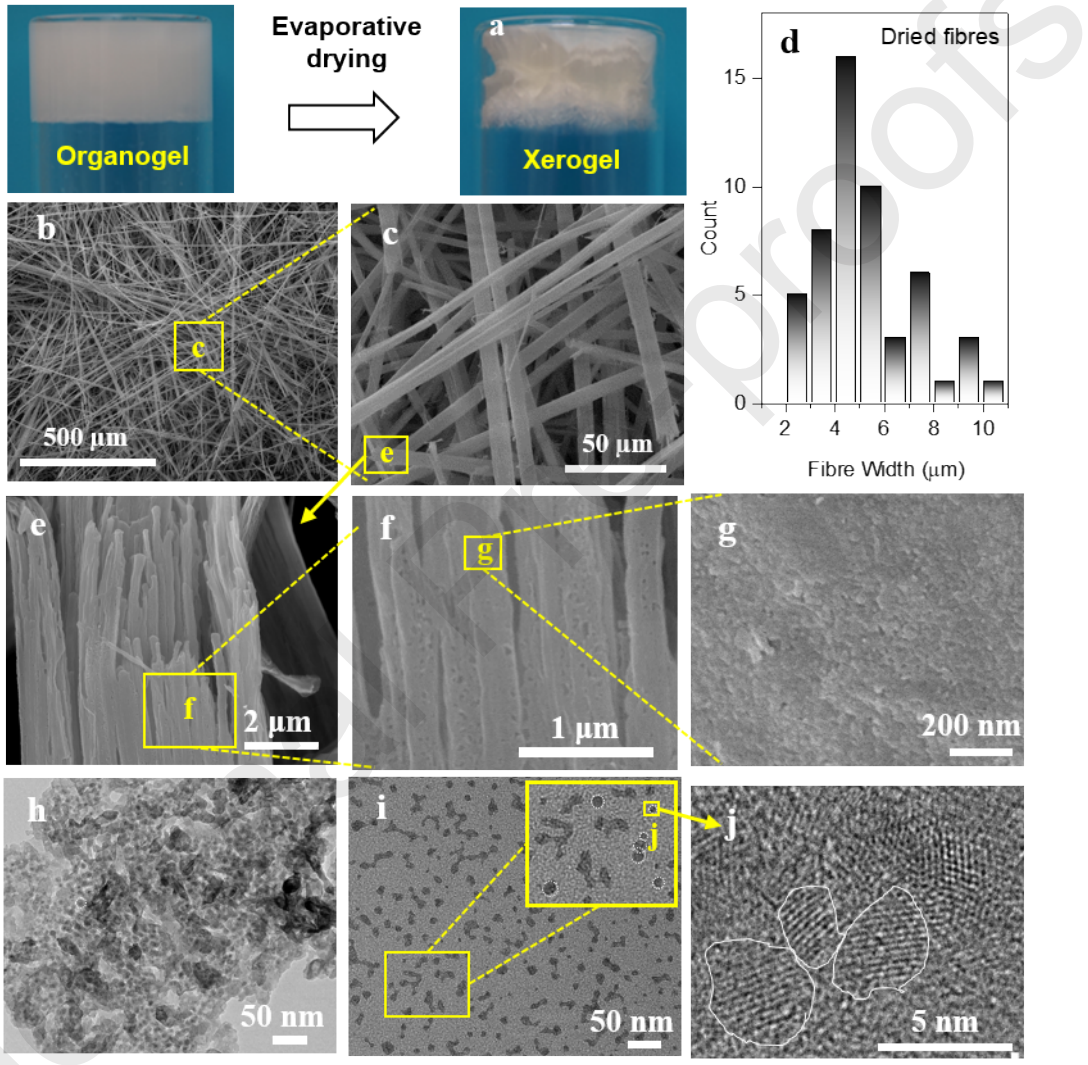

Fig. 2 Microstructural analyses of xerogel fibers. a, Xerogel after further 15 days of evaporation of the organogel in Fig. 1c with the dried microfibrillar network shown in **b**, and an enlarged view of the yellow rectangle region in **b** shown in **c**. **d**, The width distribution in the range 2-11 µm of the dried microfibres in **b**. **e**, Magnified view of a broken microfiber (the yellow rectangle in **c,** rotated by 90^{O} clockwise with respect to **c**) showing constituent nanofiber bundles. **f**, Enlarged view of the nanofiber bundles in a microfibre segment (yellow rectangle in **e**). **g**, A

further magnified SEM view of a section of an individual nanofiber (the yellow rectangle in **f)**. **h**, TEM image of a microfibrillar fragment showing constituent nanocrystals. **i**, TEM image from xerogel microfibres dispersed in ethanol, with the inset showing constituent nanocrystal aggregates with several highlighted by whited dotted circles. **j**, Magnified HRTEM image showing an aggregate (the small yellow rectangle in the inset of **i**) composed of LZH nanocrystals (three of which are outlined). The sample preparation for TEM images in Fig. 2h is as follows: (1) a carbon-coated TEM grid was brought into contact with the drying fibrillar network from Fig. 2b, and (2) the carbon-coated TEM grid was purged with aurilave to remove any loose deposits[32].

Temporal structural evolution in the gelation process

The above observations indicate that the macroscopic transformation from a turbid ZnO nanofluid to an organogel is underpinned by the microstructural evolution in the evaporating solution, from ZnO nanoparticles, through LZH nanocrystals and LZH nanocrystal aggregates, to nanofibres and microfibres (*i.e.* bundles of nanofibers) in the ultimate gel. A series of time-lapsed photos of 20 mL evaporating ZnO nanofluid in a glass vial (Fig. 3) show its macroscopic transformation to organogels in a period of 218.25 h (~ 9 days). At the evaporation time of 24 h, the turbid ZnO nanofluid transformed into two phases in coexistence, with a transparent upper layer (~ 1 mL) and a turbid lower layer (Fig. 3a). At 72 h, the lower ZnO nanofluid layer became less turbid (Fig. 3b). At 120 h, an almost transparent liquid was present in the vial (Fig. 3c). If this transparent liquid was kept hermetically, it would remain stable, appearing transparent for at least three months; we thus term it *transparent stable suspension* (TSS). At 168 h, a completely transparent liquid was observed (Fig. 3d). At the evaporation time of 216 h, the transparent liquid was further concentrated but no precipitation was observed (Fig. 3e). At 218 h, a gel phase emerged at the top layer (Fig. 3f), then

rapidly throughout the vial after just 15 min (Fig. 3g-i).

The temporal evolution of the constituent nanostructures in the evaporating nanofluid was followed by Cryo-TEM imaging to shed light on the hierarchical self-assembly for the gel fibres. Cryo-TEM (Fig. 3a1) of the transparent upper phase at 24 h evaporation time (cf. Fig. 3a) showed a small number of globular aggregates of size < 15 nm (with a few aggregates indicated by the arrows in Fig. 3a1 inset) and TEM/HRTEM further revealed LZH nanocrystals of size 1.6-3.2 nm in the upper phase after ultracentrifugation (Supplementary Fig. S2A, B), in close agreement with the size of the nanocrystals constituting microfibres (Fig. 2j).

An appreciable number of nanocrystal aggregates of size < 25 nm (denoted by arrows in Fig. 3b1) emerged in the transparent upper layer at 72 h, slightly bigger than those packed in xerogel microfibers (Fig. 2e) due to solvation. This LZH nanocrystal aggregate suspension remained stable against aggregation and precipitation for at least 3 months. These nanocrystal aggregates formed as a result of the balance between entropic and van der Waals attraction, and the repulsion between short carbon chain of isobutylamine adsorbed on the surface of LZH through hydrogen bonds between isobutylamine and oxygen atom in LZH nanocrystals. Similarly, such an equilibrium cluster phase has recently been reported in protein solutions[38] and colloid-polymer mixtures [39, 40] through the combination of the repulsive interactions with the short-range attraction.

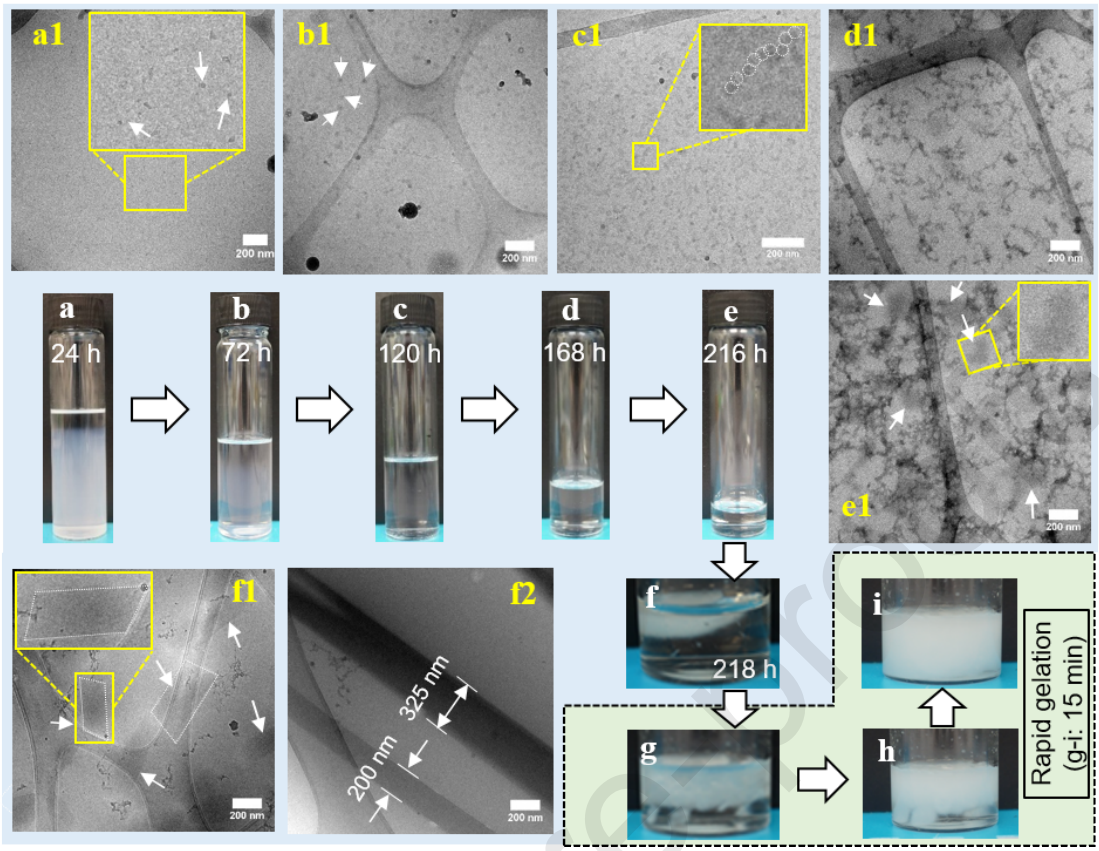

Fig. 3 Photos of a slowly evaporating ZnO dispersion in a vial and corresponding Cryo-TEM images revealing evolution of the nanofluid into microfibrillar gels. Evaporation time: (**a**) 24 h, (**b**) 72 h, (**c**) 120 h, (**d**) 168 h, (**e**) 216 h, and (**f**) 218 h when gelation initiation occurred at the top layer of the transparent stable suspension (TSS), followed by rapid gelation within 15 min (**g-i**). **a1-e1,** Cryo-TEM images of the transparent liquid in the *upper* phase in Fig. 3a-e, respectively. The arrows in **a1** (24 h) inset indicate the presence of globular aggregates of size < 15 nm, whilst an appreciable number of nanocrystal aggregates of size < 25 nm was observed in **b1** (72 h) as indicated by the arrows. In **c1** (120 h), linear assemblies of nanocrystal aggregates were observed in the TSS, and the inset highlights an example (dotted circles). In **d1** (168 h), multibranched network was observed composed of short linear assemblies of nanocrystal aggregates, and the network became denser upon further evaporation (**e1**, 216 h). Here, destabilization of the TSS triggered rapid nucleation through reorganization of nanocrystal aggregates, with several nucleating aggregates indicated by the arrows, and a magnified nucleating aggregate shown in the inset. Short fibres would then form by anisotropic 1D growth from the nucleation sites, rather than aggregation into large precipitating

agglomerates. **f1** and **f2** (218 h) show the presence of short (<400 nm) and longer nanofibers, respectively, in the *lower* liquid phase of the gelatinized TSS in Fig. 3f. All the scale bars in the Cryo-TEM images correspond to 200 nm. The vial was shaken by hand (inverting it repeatedly) every 12 h. For Cryo-TEM, the transparent liquid in the upper phase in the vial (Fig. 3a-f) was extracted with a micro-pipettor and plunge-frozen by an FEI Vitrobot™ Mrak IV, and the frozen specimen was then analysed in the microscope using a Gatan Cryo-Transfer specimen holder.

With the solvent evaporation, the volume fraction of the nanocrystal aggregates gradually increased in the evaporating solution. Some nanocrystal aggregates assembled into short linear assemblies with the width of single aggregate (with a linear assembly indicated by the white circles in Fig. 3c1 inset), in coexistence with the aggregates in the TSS at 120 h evaporation time. At 168 h, Cryo-TEM revealed the prevalence of a tenuous multibranched network composed of short linear assemblies of nanocrystal aggregates in the TSS (Fig. 3d1), which then became dense disordered networks upon further evaporation (*e.g.* at 216 h in Fig. 3e1). The TSS with multibranched networks was still transparent and stable, indicating a dynamic equilibrium exchange between nanocrystal aggregates in solvent and the aggregate networks.

With further 2h evaporation, gelation was initiated in the top layer of the solution in the vial (Fig. 3f), with short nanofibers (length < 400 nm) as indicated by the arrows and dotted outlines (Fig. 3f1; also an enlarged view in the inset) and long nanofibres (Fig. 3f2) present in the lower gelatinized TSS phase. The widths of the two nanofibers in Fig. 3f2 were 200 nm and 325 nm, respectively, comparable to those in the nanofiber bundles. This indicates that, with the TSS further concentrated, the destabilization of TSS triggered rapid nucleation of nanofibers through reorganization of

nanocrystal aggregates (several nucleating aggregates indicated by white arrows in Fig. 3e1 and a magnified nucleating aggregate in the inset of Fig. 3e1), rather than aggregation into large precipitating agglomerates. The short nanofibres then formed in numbers (indicated by arrows in Fig. 3f1). Subsequent fibre growth could result from the coupling of short nanofibres as they consumed nanocrystal aggregates. The reorganization of nanocrystal aggregates in the dense networks into well-defined nanofibers is entropically and energetically favored[41]. Compared to the loose multibranched networks of nanocrystal aggregates, the well-defined nanofibers are composed of closely packed nanocrystal aggregates in an entropy-driven ordered phase, thereby reducing the interfacial energy between the nanocrystal aggregates and the solvent. Subsequently, the nanofibres were further bundled into rigid microfibres spontaneously, to further minimise the free energy of system. Both the van der Waals attraction and the repulsion of short carbon chain of isobutylamine stationed on microfibres provide an effective cross-linking driving forces, resulting in the formation of the gel phase. Due to the evaporation-induced concentration gradient of nanocrystal aggregates from the interface towards the lower section of the vial, the gel phase formation was initiated from the interfacial zone, propagating to the bottom of the vial.

Proposed gelation mechanism: From nanofluids, through in situ-generated nanocrystals, to anisotropic growth of nanofibers and microfibres

Based on the above analysis, a three-stage mechanism to account for the macroscopic and microscopic structural evolution from the nanofluid into gels upon solvent evaporation is shown schematically in Fig. 4. In the first *pre-nucleation clustering stage* (**1**), LZH nanocrystals with intercalated isobutylamine (Fig. 4b3) formed from the hydration-dissolution of ZnO nanoparticles

assemble into nanocrystal aggregates, resulting in the TSS, with the dynamic exchange between nanocrystals and nanocrystal aggregates (Fig. 4b1). Then the multibranched nanocrystal aggregate networks (Fig. 4b2) form in the TSS upon further evaporation. In the subsequent second *nucleation and 1D anisotropic nanofibre growth stage* (**2**), the concentrated TSS triggers the nucleation and 1D growth of nanofibres through reorganization of the nanocrystal aggregates (Fig. 4c1), forming short nanofibers (Fig. 4c2) which couple to form longer nanofibers (Fig. 4c3). Such anisotropic 1D growth preferentially along the LZH (001) direction is quite unusual, and is underpinned by the mesolamellar structure of the *in situ*-generated nanocrystals, with the anisotropic stacking mediated by the isobutylamine layer on the (001) crystal facet which provides a larger accessible area to template isobutylamine adsorption, compared to the crystal edges. In the final *rapid gelation stage*, the nanofibres rapidly bundle into microfibres (Fig. 4d1), leading to the 3D microfibrillar networks in ultimate gel. It is tempting to argue that the microfibre width is an outcome of free energy minimisation of the self-assembly process. However, considering the non-equilibrium nature of the process, it is more likely that it is limited by the local nanofibre concentration, which could be tuned by ZnO particle morphology and crystallinity that affects the *in stiu*-generated ZnO hydration-dissolution process and thus the LZH nanocrystal concentration[31]. The process from the TSS (with multibranched aggregate networks, Fig. 4b2) to the ultimate gel (Fig. 4d) is a thermally reversible process, with the gel rapidly dissolving into a solution upon moderate heating and re-gelation upon cooling. Such thermal reversibility confirms that the physical driving force for nanofiber and microfibre growth *via* self-assembly of nanocrystal aggregates is of the order kT (thermal energy), and the spontaneous nature of the anisotropic self-assembly process for the fibre formation.

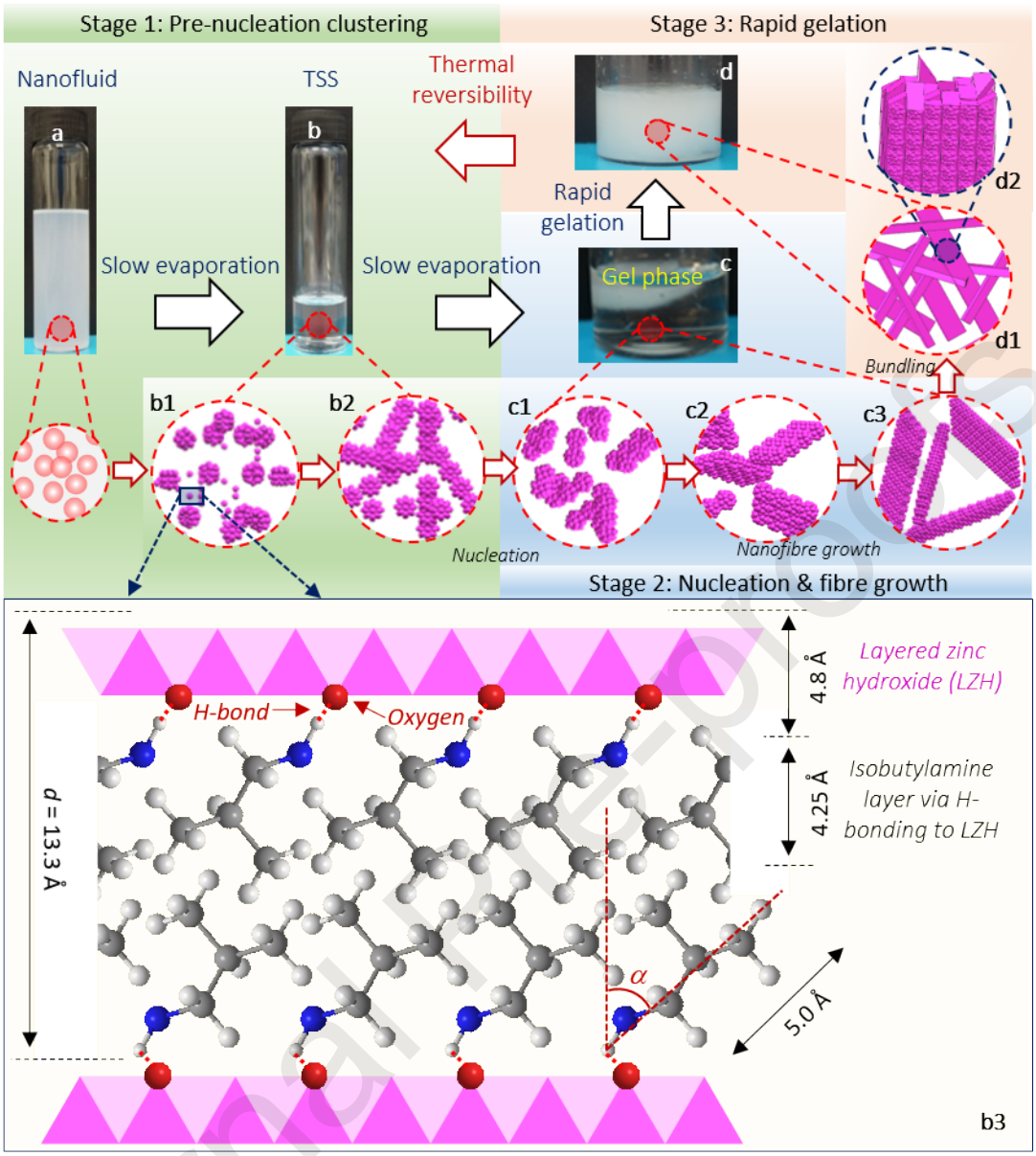

Fig. 4 Schematic representation of a macroscopic and microstructural evolution from nanofluids into gels with hierarchical microfibrillar networks upon solvent evaporation. Stage 1: The pre-nucleation clustering stage. **a**, ZnO nanofluids. **b**, Transparent stable suspensions (TSSs) with the dynamic exchange between LZH nanocrystals (**b3**) and nanocrystal aggregates (**b1**), and with multibranched nanocrystal aggregate networks (**b2**); **Stage 2**: Nulceation and fibre growth. **c**, Gel phase formation initiated from the solution-air interface zone and propagating downwards; (**c1**) nucleating aggregates from reorganization of the aggregates in the TSS, forming short nanofibers (**c2**) and longer nanofibers (**c3**). **Stage 3: Rapid gelation. d**, Microfibrillar gels comprising microfibrillar networks (**d1**), with the microfibres consisting of nanofibre bundles (**d2**).

Conclusions

In summary, our results demonstrate that the hierarchical microfibrillar nanocrystal gel can be anisotropically self-assembled from *in situ*-produced LZH nanocrystals *via* a facile solvent evaporation route without pre-functionalization or stabilization ligands. This microfibrillar nanocrystal gel is thermally reversible, reverting to a liquid upon modest heating and re-gelling rapidly upon cooling. The anisotropic assembly of gel fibers proceeds through *in situ*-produced LZH-isobutylamine nanocrystals, nanocrystal aggregates, multibranched aggregate networks, nanofibres to ultimate microfibres, manifested on a macroscopic level as the cloudy ZnO nanofluid transferring into the final gel phase through a transparent stable suspension upon solvent evaporation. Whilst our results demonstrate facile fabrication of LZH-NC gels comprising 1D assemblies of nanocrystals, the mechanism we have elucidated has broad implications to nanofluids[42-44] containing other reactive metal oxide particles (*e.g.* CdO, HgO, SrO, MnO, and CuO) which have also been observed to exhibit the tendency for anisotropic fibre growth from evaporation-induced self-assembly (ms. in preparation). Our results may also open up routes for the incorporation of other nanocrystals (such as noble metal nanocrystals, TiO_2, SiO_2, Y_2O_3 and ZrO_2) or carbon nanomaterials into inorganic fibrillar networks to fabricate hybrid gels. Such inorganic fibrillar gels may be exploited for applications in photocatalysis and solar cell[45], as well as for inorganic-organic hybrid gels, *e.g.* with interpenetrating inorganic-organic double-networks. It might also be interesting to apply the fabrication route to oil-in-water microemulsions to prepare nanocrystal micro/nanogels. In our experiment, we have used the slow evaporation rate (and thus the quasi-equilibrium condition) to suppress solvent flows and instabilities observed under fast dynamic

evaporation conditions[31-33]. It remains an interesting prospect to further investigate potentially accelerating the gelation process, *e.g.* under elevated temperatures or reduced pressures.

References

1. C. Ziegler, A. Wolf, W. Liu, A. K. Herrmann, N. Gaponik and A. Eychmuller, *Angewandte Chemie*, 2017, **56**, 13200-13221.
2. D. Wen and A. Eychmüller, *Chem. Commun.*, 2017, **53**, 12608-12621.
3. W. C. Wan, R. Y. Zhang, M. Z. Ma and Y. Zhou, *J. Mater. Chem. A*, 2018, **6**, 754-775.
4. F. Rechberger and M. Niederberger, *Nanoscale Horiz.*, 2017, **2**, 6-30.
5. C. A. Saez Cabezas, G. K. Ong, R. B. Jadrich, B. A. Lindquist, A. Agrawal, T. M. Truskett and D. J. Milliron, *Proceedings of the National Academy of Sciences of the United States of America*, 2018, **115**, 8925-8930.
6. T. Berestok, P. Guardia, M. Ibanez, M. Meyns, M. Colombo, M. V. Kovalenko, F. Peiro and A. Cabot, *Langmuir*, 2018, **34**, 9167-9174.
7. V. Sayevich, B. Cai, A. Benad, D. Haubold, L. Sonntag, N. Gaponik, V. Lesnyak and A. Eychmuller, *Angewandte Chemie*, 2016, **55**, 6334-6338.
8. A. Singh, B. A. Lindquist, G. K. Ong, R. B. Jadrich, A. Singh, H. Ha, C. J. Ellison, T. M. Truskett and D. J. Milliron, *Angewandte Chemie*, 2015, **54**, 14840-14844.
9. A. Wolf, V. Lesnyak, N. Gaponik and A. Eychmuller, *The journal of physical chemistry letters*, 2012, **3**, 2188-2193.
10. J. L. Mohanan, I. U. Arachchige and S. L. Brock, *Science*, 2005, **307**, 397-400.
11. N. C. Bigall, A. K. Herrmann, M. Vogel, M. Rose, P. Simon, W. Carrillo-Cabrera, D. Dorfs, S. Kaskel, N. Gaponik and A. Eychmuller, *Angewandte Chemie*, 2009, **48**, 9731-9734.
12. X. Gao, R. J. Esteves, T. T. Luong, R. Jaini and I. U. Arachchige, *Journal of the American Chemical Society*, 2014, **136**, 7993-8002.
13. K. S. Subrahmanyam, C. D. Malliakas, S. Debajit, G. S. Armatas, J. S. Wu and M. G. Kanatzidis, *J. Am. Chem. Soc.*, 2015, **137**, 13943-13948.
14. S. Bag, A. F. Gaudette, M. E. Bussell and M. G. Kanatzidis, *Nat. Chem.*, 2009, **1**, 217-224.
15. P. Mohapatra, S. Shaw, D. Mendivelso-Perez, J. M. Bobbitt, T. F. Silva, F. Naab, B. Yuan, X. Tian, E. A. Smith and L. Cademartiri, *Nat. Commun.*, 2017, **8**, 2038-2044.
16. S. M. Jung, H. Y. Jung, M. S. Dresselhaus, Y. J. Jung and J. Kong, *Sci. Rep.*, 2013, **2**, 849.
17. W. Cheng, F. Rechberger and M. Niederberger, *Nanoscale*, 2016, **8**, 14074-14077.
18. Z. Y. Tang and N. A. Kotov, *Adv. Mater.*, 2005, **36**, 951-962.
19. H. Wang, L. Chen, X. Shen, L. Zhu, J. He and H. Chen, *Angewandte Chemie*, 2012, **51**, 8021-8025.
20. M. Grzelczak, J. Vermant, E. M. Furst and L. M. Liz-Marzan, *ACS Nano*, 2010, **4**, 3591-3605.
21. K. Liu, Z. Nie, N. Zhao, W. Li, M. Rubinstein and E. Kumacheva, *Science*, 2010, **329**, 197-200.
22. H. Jie, Y. J. Liu, T. Babu, Z. J. Wei and Z. H. Nie, *J. Am. Chem. Soc.*, 2012, **134**, 11342.
23. Z. Y. Tang, N. A. Kotov and M. Giersig, *Science*, 2002, **297**, 237-240.
24. Z. Zhang, Z. Y. Tang, N. A. Kotov and S. C. Glotzer, *Nano Lett.*, 2007, **7**, 1670-1675.

25. K. Miszta, G. J. De, G. Bertoni, D. Dorfs, R. Brescia, S. Marras, L. Ceseracciu, R. Cingolani, R. R. Van and M. Dijkstra, *Nat. Mater.*, 2011, **10**, 872-876.
26. X. Du, J. Zhou, J. Shi and B. Xu, *Chem. Rev.* , 2015, **115**, 13165-13307.
27. P. Terech and R. G. Weiss, *Chem. Rev.*, 1997, **97**, 3133-3160.
28. L. E. R. O'Leary, J. A. Fallas, E. L. Bakota, M. K. Kang and J. D. Hartgerink, *Nat. Chem.*, 2011, **3**, 821-828.
29. L. C. Palmer and S. I. Stupp, *Acc. Chem. Res.*, 2008, **41**, 1674-1684.
30. P. Jonkheijm, P. V. D. Schoot, A. P. H. J. Schenning and E. W. Meijer, *Science*, 2006, **313**, 80-83.
31. P. Wasik, C. Redeker, T. G. Dane, A. M. Seddon, H. Wu and W. H. Briscoe, *Langmuir*, 2018, **34**, 1645-1654.
32. H. Wu and W. H. Briscoe, *Phys. Rev. Mater.*, 2018, **2**, 045601.
33. H. Wu, L. X. Chen, X. Q. Zeng, T. H. Ren and W. H. Briscoe, *Soft Matter*, 2014, **10**, 5243-5248.
34. M. I. Baneyeva and S. V. Popova, *Geochem. Int.*, 1969, **8**, 807-809.
35. C. H. Liang, Y. Shimizu, M. Masuda, T. Sasaki and N. Koshizaki, *Chem. Mater.*, 2004, **16**, 963-965.
36. A. kasai and S. Fujihara, *Inorg. Chem.*, 2006, **45**, 415-418.
37. F. Song and X. Hu, *Nat. Commun.*, 2014, **5**, 4477-4486.
38. A. Stradner, H. Sedgwick, F. Cardinaux, W. C. K. Poon, S. U. Egelhaaf and P. Schurtenberger, *Nature*, 2004, **432**, 492-495.
39. F. Sciortino, S. Mossa, E. Zaccarelli and P. Tartaglia, *Physical review letters*, 2004, **93**, 055701.
40. J. Bergenholtz, W. C. K. Poon and M. Fuchs, *Langmuir*, 2003, **19**, 4493-4503.
41. K. J. Bishop, C. E. Wilmer, S. Soh and B. A. Grzybowski, *Small*, 2009, **5**, 1600-1630.
42. W. H. Briscoe, *Curr Opin Colloid In*, 2015, **20**, 46-53.
43. G. A. Pilkington and W. H. Briscoe, *Adv Colloid Interfac*, 2012, **179**, 68-84.
44. G. A. Pilkington, J. S. Pedersen and W. H. Briscoe, *Langmuir*, 2015, **31**, 3333-3342.
45. L. Mohapatra and K. Parida, *J. Mater. Chem. A*, 2016, **4**, 10744-10766.

Conflicts of interest

There are no conflicts of interest to declare.

Acknowledgements

H.W. would like to acknowledge funding from Marie Skłodowska-Curie Individual Fellowships (Project Number 656830). W.H.B. would like to acknowledge funding from the Engineering and Physical Sciences Research Council (EPSRC) (EP/H034862/1, EP/G036780/1, EP/L016648/1, EP/K502996/1, EP/J500379/1) and FP7-PEOPLE-2011-ITN - Marie-Curie Action: "Initial Training Networks" (MCITN) (NanoS3, Grant No. 290251). The authors would especially like to thank J. Mantell (Faculty of Biomedical Sciences, University of Bristol) for the Cryo-TEM

measurements.

Graphic ToC